Compact outflows associated with TMC1 and TMC1A

C. J. Chandler

Mullard Radio Astronomy Observatory, Cavendish Laboratory, Madingley Road,

Cambridge CB3 0HE, United Kingdom

S. Terebey

Infrared Processing and Analysis Center, Jet Propulsion Laboratory and California

Institute of Technology. $^{\prime}$A$_{=}$$^{\prime}$ 00-22, Caltech, Pasadena CA 91125

M. Barsony[1]

Physics Department, University of California, Riverside, CA 92521

T. J. T. Moore

School of Electrical Engineering, Liverpool John Moores University, Byrom Street,

Liverpool L3 3AF, United Kingdom

a id

T. N. Gautier

Jet Propulsion Laboratory, MS 169-327, 4800 Oak Grove Drive, Pasadena CA 91109

ABSTRACT

High spatial resolution observations are presented of the compact outflows associated with the young protostars TMC1 (IRAS 04381+2540) and TMC1A (IRAS 04365-2535) in Taurus. Emission in CO(1-0) imaged with the Owens Valley millimeter array shows the outflow lobes to be conical close to the star. Analysis of the outflow dynamics indicates that these objects are low-luminosity versions of the energetic outflows more commonly observed. Near-infrared images at H and K show a close correspondence between reflection nebulosity and the location of high-velocity gas, and suggest the outflow cavity is evacuated, as do])ositio])-velocity" diagrams of the CO(2-1). Comparison of the J= 1- 0 transition with emission in the 2-1 line indicates that the excitation temperature in the high-velocity gas is higher than the surrounding Taurus cloud. We place limits on the inclination of both objects by comparing the data with theoretical outflow models, and conclude that $i \sim$ 40 70° for both objects. The deprojected opening angles of the outflow cones are then in the range 30 40°.

None of the current outflow models satisfactorily explains the results for TMC1 and TMC1A, which are among the youngest Class I sources in Taurus. We find their outflow structure shares many similarities with the more obscured and possibly younger Class 0 objects, B335 and L1448-C. The main difference is the lower mechanical luminosities of the TMC1 and TMC1A outflows, reflecting a factor of 3 4 smaller linear extent and velocity, and factor of 10 20 lower mass than the L1448 C molecular jet source. Taken together, the four protostars share the common properties of 1) conical outflow lobes close to the star, 2) evacuated outflow cavities, and 3) relatively wide 3() 45° opening angles. A successful theory of young stellar outflows must be able to explain these characteristics.

Subject headings: stars: formation ISM: j e t s and out flows reflection nebulae

St/al's: individual: TMC1, TMC1 A

1. Introduction

All stars are thought to go through a phase of energetic mass loss during their formation, most commonly observed as high-velocity molecular outflows. It is still not clear How the outflows are driven, nor how the molecular gas is accelerated, yet it is essential to understand outflows if star formation in general is to be understood.

A common outflow mechanism in both low and high-mass sources is implied by the good correlations found between the bolometric source luminosity and outflow momentum flux and outflow mechanical luminosity for young stars (Bally & Lada 1983; Edwards, Ray, & Mundt 1993; Cabrit & Bertout 1992). If there is a common mechanism we might expect the physical and dynamical properties of outflows from low and high mass objects to be similar. Recent models for the driving of molecular outflows (e.g., Shu et al. 1991; Masson & Chernin 1992, 1993; Stahler 1994) have begun to make definite predictions for the observed structure of outflows, particularly close to the exciting star. High spatial resolution observations of the outflows from nearby protostars, which are predominantly low- mass, therefore have the potential to distinguish between different models.

The strongest constraints 011 the driving and acceleration mechanisms of outflows are best obtained through observations of young, unevolved outflow's, where the cloud core has not yet been significantly dispersed by the process of star formation. Statistical arguments indicate that outflows start when the central protostar is less than a few $\times 10^4$ years old (Parker, Padman, & Scott 1991), as does the recent study of VLA1623 (André, Ward-Thompson, & Barsony 1993). We might therefore hope to find the youngest, least- evolved outflows from the protostars which have not yet accumulated much mass.

To try to distinguish between various models for the outflow driving mechanism and the acceleration of ambient gas, we have carried out a detailed, high-resolution study of two young, embedded sources in the nearby Taurus star-forming region: TMC1 (1RAS

04381-12540) and TMC1A (IRAS 04365-12535). They have the steepest 2 to 25 μm spectral index of the objects in Taurus surveyed in the infrared by Myers et al. (1987), suggesting that they are two of the youngest and most deeply embedded sources in this region, and have luminosities of 0.73 $L_\odot$ and 2?.4 $L_\odot$ respectively. Both objects were originally reported not to have outflows in large-beam, single-dish surveys, but were shown to have high-velocity, compact emission in the interferometer snapshot survey of Terebey, Vogel, & Myers (1989). They are therefore good candidates for having young, compact, unevolved outflows.

To study the energetics of the high-velocity gas in TMC1 and TMC1A, and to examine its small-scale structure, we have performed high-resolution imaging of both sources in CO $J: 1-0$ and $J= 2-1$, and in the near-infrared continuum. Below we describe the results and compare our data with predictions from recent outflow models, providing new constraints on the driving mechanism of outflows.

2. Observations and data reduction

2.1. CO $J= 1-0$ observations using the Owens Valley Millimeter Array

Full aperture synthesis maps of TMC1 and TMC1A in CO $J= 1-0$ were made using the Owens Valley Millimeter Array during the period 1988 January to June. The absolute flux scale was established from observations of the planets, and results in an estimated uncertainty of 15%. Spectral line data were obtained using a filter bank with 32 channels at 1 MHz (2.6 km s^{-1}) resolution. After calibration, the data were imaged using the AIPS reduction package. The resolutions (FWHM) of the CO beam made with uniform weighting, were $7.0 \times 6.8''$ at PA 28° for TMC1A and $7.3 \times 6.6''$ at PA 8° for TMC1. The rms noise in each channel is 0.38 Jy/beam for TMC1A, and 0.15 Jy/beam for TMC1.

2.2. CO $J = 1-0$ observations using the NRAO 12-m

A single-dish spectrum of the CO $J = 1-0$ emission from TMC1 A was made in 1991 April using the 1 ?-m telescope of the National Radio Astronomy Observatory[2] at Kitt 1 'eak. The velocity resolution was 0.1 27 km s^{-1} and the beam was 60" at 2.7 mm. Monitoring of the pointing and focus showed they were good to 15" and 10%, respectively. The data were corrected for forward scattering and spillover on-line to give spectra of T_R^*. Observations Of the flux calibration source Orion A showed the absolute calibration of T_R^* was within 1 0 % and flux repeatability was 5%. Since T_R^* refers to a source extended relative to the main beam, and the emission from TMC1 A is relatively compact compared with 60" (see § 3), we have further corrected our data to main beam brightness temperature, T_{MB} by dividing by 0.82 (P. Jewell, private communication).

2.3. CO $J = 2-1$ observations using the JCMT

The CO $J = 2-1$ observations of TMC1 and TMC1 A were carried out at the 15 m James Clerk h4 axwell Telescope (JCMT), on Mauna Kea, 11 awaii. TMC1 A was observed in 1990 September, and TMC1 in 1991 September. 110{11 Sets of observations Used the common-user Schottky receiver, and an acousto optical spectrometer (AOS) with a channel spacing of 250 kHz, and a resolution of 330 kHz. The beam width at 230 GHz is about 21". Typical double-sideband system temperatures were 1000 - 2000 1<. Integration times of around 400 seconds, including on and off positions, yielded an rms noise (in units of T_A^*) of 0.24 I{ per channel. The pointing was checked using CRL618 every 1-2 hours, and was found to be good to 5".

An off-position 10 arcminutes east of the program source was adopted in each case. Since the Taurus cloud is so extended, it is difficult to find a good c]~lissio]i-free region to use as an off position. To maintain reasonable baselines we were restricted to using a position relative] y close to each source. There is therefore a serious possibility of emission at the off position. However, since we are interested mainly in the Higl)-velocity emission away from the cloud systemic velocity, we have made no attempt to correct the resulting 011- oft" spectra for emission in the off-beam. The maps are fully-sampled, with a point spacing of 10". 1)ue to time constraints during the observing, we concentrated on mapping only the main, extended outflow lobe in each source (i.e., the blue lobe in TMC1A and the red lobe in TMC1). We also obtained spectra at offsets of 30" from the central source in the direction of the opposite lobe, but no Hit~]-velocity emission was found in either case.

The data reduction and ii]].aF;e processing were carried out using SPECX and A IPS. In order to compare the single-dish data directly with the interferometer maps, we have converted the JCMT spectra. from units of T_A^* to Jy/beam. A linear baseline has been removed from all the spectra, which have then been corrected for forward scattering and spillover by dividing by $\eta_{fss} = 0.8$ to give T_R^*, and multiplied by 19 Jy/beam/K. The rms noise per channel is therefore 5.7 Jy/beam.

2.4. Near-infrarm] imaging at the Hale 5-m telescope

Neal-illfrared H and K images of TMC1 and TMC1 A were obtained in 1988 December using the PFIRCAM infrared camera mounted at the prime focus of the Hale 5-m telescope on Mount 1 'alomar. The camera used a 128 x 128 HgCdTe detector array bonded to a Reticon readout and operating between 1 and 1.5 μm with 0.765" pixels. The spatial resolution of the observations, determined by the seeing, was about 1.5". The data were taken alternating between the source and four different sky positions. The images were

bias-subtracted, and then flat-fielded with a median sky frame, using special IDL software developed for PFIRCAM. The total oJI-source integration times of the final images were 880 seconds at K and 240 seconds at H for TMC1, and 1000 seconds at K and 1280 seconds at H for TMC1 A. The image.s have also been smoothed to approximately 2.5″ resolution. Photometric standards were selected from the CIT system (Elias et al. 1982).

The data were not obtained under photometric conditions. However, the quality is sufficient to study source structure. Careful monitoring of the sky background showed good stability for both TMC1 and TMC1 A at both H and K. A comparison with published fluxes shows agreement within 0.4 magnitudes. Near-il}framd images that have been published previously for TMC1 and TMC1 A (Kenyon et al. 1993b; Tamura et al. 199]) arc less sensitive and have lower spatial resolution. The images presented here reveal the underlying structure of the extended nebulosity.

3. lh'suits

3.1. Molecular line emission

5',1.1. Morphology

in Figures 1 and 2 we compare Owens Valley CO(1 - 0) channel data with the JCMT CO(2- 1) data, which have been averaged over 8 channels to give the same spectral resolution as the it iterferometer im ages. The LSR velocity is marked at the top right of each panel, in km s‘. The position of the millimeter continuum source from Terebey, Chandler, & André (1 993) is marked by an asterisk in each image, and the scale is the same in each data set. Both TMC1 and T MC1 A show distinct red- and blue-shifted lobes oriented north - south . Features larger than 20″ visible in the single-dish data are resolved out by the interferometer. A comparison with the NRAO 12-m spectrum of TMC1 A shows that

the interferometer has resolved out over 50% of the total flux density in the line wings of that source, and more than 90% of the flux close to the systemic velocity. Nevertheless, the correspondence between the locations of the small-scale structure in lint]] the JCMT and Owens Valley data sets, in the different transitions of CO, is extremely good. The systemic LSR velocity measured by Terebey et al. (1989) is 5.5 km s^{-1} for TMC1 and 6.4 km s^{-1} for TMC1A.

At high resolution in the interferometer data, the TMC1A outflow (Figure 2a) shows the blue lobe at 4- i' 1{111 away from the systemic velocity to have a conical structure, with its apex located at the position of the millimeter continuum source. A similar, less extended structure is also seen in the red-shifted channel. The red lobe of TMC1 (Figure 1a) is also roughly conical, with the highest velocity emission at the largest distance from the source. This is more clearly demonstrated in the CO(2- 1) JCMT data (Figure 1b), where the peak in the emission shifts about 20'' south moving from $V_{LSR} = 6.8$ km s^{-1} to V_{LSR} ' 19.7 km s^{-1}. This is also seen, to a slightly lesser degree, in the blue lobe of TMC1A traced by CO(2- 1) (Figure 2b).

The integrated red and blue CO(1 - 0) emission (Figure 3) demonstrates the conical structure of the outflow lobes, extending to within 1000 AU of the continuum source. In Figure 4 we directly compare these interferometer results (given in greyscale) with the integrated JCMT CO(2- 1) emission (contours). All the features in the high-resolution data have corresponding emission in the CO(2- 1) maps. The orientation of both outflows is similar, with position angles for the outflow axis of 0° for TMC1 and - 10° for TMC1 A. Because of their larger spatial coverage and higher spectral resolution we use the CO(2- 1) data to analyze the dynamics of the outflow

3.1.2. *Optical depth and excitation temperature of the CO*

For TMC1 A we have combined information from the single-dish CO $J = 1-0$ spectrum, tile Owens Valley images, and the $J = 2-1$ data to derive constraints on the optical depth and the excitation temperature of the CO emission in the outflow wings. First, consider the two single-dish data sets. The CO(1-0) spectrum obtained using the NRAO 12-m has been smoothed and resampled to have the same spectral resolution as the $J = 2-1$ JCMT data, while the 2-1 data were smoothed spatially to match the 12-m beam. The resulting spectra are displayed in Figure 5, with a clotted line denoting the (2-1)/(1-0) line ratio (T_{21}/T_{10}) in the region where the signal-to noise ratio was greater than unity in both transitions. In the line wings T_{21}/T_{10} has a mean value of 2.3, or equivalently, a flux density ratio S_{21}/S_{10} of 9.3. This can be translated into a lower limit to the excitation temperature in the high-velocity gas by assuming LTE and optically-thin emission. Figure 6 shows the predicted value of S_{21}/S_{10} as a function of T_{ex} for various optical depths in the $J = 1$-0 line, τ_{10}, assuming LTE (note that $\tau_{21} > \tau_{10}$ as long as $T_{ex} > 5.5$ K). In the optically-thin limit the minimum excitation temperature that can be responsible for the observed flux density ratio, denoted by the dotted line, is 20 K. This temperature is somewhat higher than the ~ 10 K observed for the bulk of the Taurus molecular cloud (Murphy & Myers 1985).

Further constraints on the excitation conditions on the scales imaged by the interferometer can be obtained by comparing the flux density in the Owens Valley CO(1 - O) maps with the CO(2-1) data. For TMC1 A, the average ratio S_{21}/S_{10} in the line wings integrated over the area of emission in the Owens Valley maps is approximately (i (solid circle, Figure 6). Since the interferometer flux density is a lower limit, this line ratio is an upper limit to the true line ratio on small scales. The difference between the line ratios derived from the large-scale, single-dish data and those obtained from the interferometer measurements reflects the {Iifl'['mill gas components sampled by the various instruments. It

demonstrates that the more extended emission to which the interferometer is not sensitive, but which is detected by the NRAO 12-m and the JCMT, either has a higher excitation temperature or is more optically thin than the compact structures. Since there is no reason to believe that the gas observed by the Owens Valley array is cooler than the material on larger scales, we assume that the result $T_{ex} \gtrsim 20$ K derived above from the large-scale emission can be applied to the more compact shut.tures. An examination of Figure 6 then shows that the emission in both the 1-0 and 2-1 transitions must be optically thick in TMC1 A. For TMC1 the ratio $S_{21}/S_{10} \sim 10$, so either $1:-.>231<$, or the interferometer has resolved out too much emission for a reasonable comparison between the two lines to be made. The latter is most likely to be the case.

The peak brightness temperature of the line wings in our data set is 6 K, and lies in the Owens Valley CO(I - O) map of TMC1A at $V_{LSR} = 2.0$ km s^{-1}. Since the excitation temperature is probably greater than 20 K, and the emission is optically thick, the observed brightness temperature implies that the emission in the outflow is clumpy even with respect to the interferometer beaI-J.

3.3.3. *Outflow properties*

In LTE the tots] mass M of molecular material is obtained from the CO(2-1) emission using the relation

$$M = 2.93 \times 10^{-8} (T_{ex} + 0.9) e^{16.6/T_{ex}} \frac{\tau_{21}}{(1 - e^{-\tau_{21}})} \left(\frac{D}{140 \text{ pc}}\right)^2 \int S dV \qquad M_\odot. \qquad (1)$$

Equation 1 assumes a mean molecular weight for the molecular gas of 1.36, and a CO abundance relative to H_2 of 10^{-4}. D is the distance to the source, and the integrated CO(2-1) flux is in units of Jy km s^{-1}. In calculating the mass of molecular material we have assumed $T_{ex} = 20$ K and $\tau_{21} << 1$. These values for the mass should therefore be regarded

as lower limits, since it is likely that $T_x > 26$ K and that the $J = 2$-1 emission is optically thick.

The detailed modeling reported by Cabrit & Bertout (1990) suggests that the best estimates for the properties of an outflow are obtained by (i) calculating the mass correcting for the line opacity, and (ii) assuming that all the material is moving at V_{max}, the maximum projected radial velocity observed, rather than the intensity-weighted velocity, $\langle V \rangle$. Since we do not know the opacity of the $J = 2$-1 emission, we have not applied any opacity correction. In Table 1 we list the dynamical timescale t_{dyn}, the momentum P, momentum flux F, energy E, mechanical luminosity L, and mass-loss rate $\dot{M}_{outflow}$ using V_{max}. Detectable emission in the 'red lobe' of TMC1 lies between 7.9 and 20.9 km s^{-1}, and the 'blue lobe' between - 3.7 and 3.4 km s^{-1}. For TMC1A the red lobe is from 7.9 to 18.3 km s^{-1}, and the blue lobe from -7.2 to 3.1 km s^{-1}. The extent R of the outflows listed in Table 1 may be larger than the area we have mapped. Many of the quantities derived are therefore limits, although emission is clearly falling off at the edge of our maps. The outflows cannot extend more than $2R$ because high-velocity gas was not detected in the lower-resolution survey of Heyer et al. (1987).

Cabrit & Bertout (1990) also calculate the error introduced by calculating outflow parameters whilst not correcting for the opacity of the CO line or inclination angle. In Table 2 we show the average error for an intermediate viewing angle, $i \sim 30$-60°. Applying these corrections to our data, the outflow momentum fluxes for TMC1 and TMC1A are in excellent agreement with those predicted by the correlation between bolometric luminosity and outflow momentum flux and mechanical luminosity found by Cabrit & Bertout (1992). The uncorrected mass-loss rates listed in Table 1 are $\sim 0.1\dot{M}_{infall}$ derived from the near-infrared colors of TMC1 and TMC1A by Kenyon et al. (1993b).

3.2. Near-infrared imaging

The results of imaging TMC1 and TMC1 A at H and K are displayed as contours in Figure 7, overlaid on greyscales of the integrated CO(1-O) emission in Figure 3. The structures we see in our K images are in good agreement with the lower sensitivity data presented by Kenyon et al. (1 993b), but we have clearly detected more of the low-level, extended nebulosity. There is an unresolved component of the near-infrared emission which we have aligned with the position of the millimeter continuum source, at the geometrical center of the outflow, since we do not have good absolute positions for the infrared measurements. The extended emission can be divided into two components. Close to the star it is roughly symmetric, while at larger distances it has more of the appearance of a unipolar reflection nebula. The most striking result, demonstrated by Figure 7 is how well this extended emission corresponds to the blue shifted outflow emission for both sources.

The structure of the near-infrared emission is in excellent agreement with Monte Carlo simulations of scattered light from embedded stars (Whitney & Hartmann 1 993; Kenyon et al. 1993b). Furthermore, our images clearly demonstrate the need for a hole or cavity to explain the extent and shape of the emission in the context of their model. We have used the photometry measured by Kenyon et al. to calibrate our images and convert them to F_ν, and find that the extended nebulosity in both sources has an intensity ratio $r = I_K/I_H \lesssim 2$, corresponding to a black-body temperature $T \gtrsim 1500$ K. Since these are low-luminosity objects the high color temperatures located at 3000 4000 AU from the central star cannot represent the physical temperature of dust at such large distances; the extended emission is most likely to be reflection nebulosity (Heyer et al. 1 990; Tamura et al. 1991 ; Kenyon et al. 19931)).

In TMC1A there is also emission at K along the northwestern edge of its nebula without corresponding features at 11, giving $r \sim 12$, and resulting in a lower color temperature of

~ 700 K at that location. Variations in the color temperature across near-infrared nebulae could be caused by two effects. First, clumpiness in the foreground extinction will have a correspondingly higher effect at H band than at K: the extinction law of Rieke & Lebofsky (1985) suggests that a K-band extinction $A_K \sim 3.2$ is needed to make an intrinsic intensity ratio of 2 appear as high as 12. Alternatively the variation in color temperature may be caused by variations in the emission mechanism across the nebula. Low values of r (and correspondingly high T) may be located in regions where the emission is predominantly reflection nebulosity, while higher intensity ratios may indicate regions of shock-heated gas, with H_2 emission contributing to the K-band flux density. Such Shocks could occur where a jet or wind driving the outflow interacts with the ambient cloud. Whatever their cause, the red knots located to the west and northwest of the star in TMC1 A may account for the apparent increase in the $H - K$ and $J - K$ colors with increasing aperture size reported by Kenyon et al. (1 993b) for this source.

It is interesting to note that where near-infrared emission is detected toward the red outflow lobe of both objects, the color of the nebulosity is similar to that in the blue. This indicates that the lack of extended emission toward the reel lobe is not clue to an increase in the la.rge-scale extinction, but must be caused either by a lack of material in the south to scatter radiation, or by the effect of forward scattering of the dust grains. The former may play an important role in TMC 1 A, where we see little molecular line emission to the south. For TM C1 though there is clearly extended molecular gas, suggesting that forward scattering is the dominant process causing the asymmetry of the red and blue lobes in the reflection nebula.

3.3. Outflow geometry and orientation

The semi-opening angle of the outflow, θ_{max}, can potentially provide important constraints on outflow models. For TMC1 and TMC1 A the well-delijlmkd conical structure permits precise measurement Of θ_{proj}, the projected semi-opening angle. We find $\theta_{proj} = 20°:12°$ for the red lobe in TMC1 , and $\theta_{proj} = 22°:1$ '2° for the blue lobe Of TMC1 A. If the wind cone is azimuthally symmetric then it is straightforward to show that

$$\tan(\theta_{max}) = \tan(\theta_{proj}) \sin i, \tag{?.}$$

where i is the inclination of the axis of symmetry to the line of sight. Values of θ_{max} derived from equation 2 are] lotted for $\theta_{proj} = 20°$ (labeled TMC1) and $\theta_{proj} = 22°$ (labeled TMC1 A) in Figure 8. We plot θ_{max} as a function of $1- \cos i$, since the probability of finding a source with inclination i is proportional to $\sin i$ and the probability distribution function is therefore proportional to $1 - \cos i$. For this choice of independent variable, equal intervals along the horizontal axis will have the same probability. Random orientations should therefore result in equal numbers of outflows below and above 60° inclination. Figure 8 demonstrates that the wind opening angle is always smaller than or equal to the projected opening angle, although the difference is primarily important for small inclinations.

The wind opening angle may therefore be computed once the inclination is known. Outflow inclinations have, however, been difficult to measure securely. outflows that are highly inclined ($i > 75°$) and lie nearly in the plane of the s k y are readily identified by their characteristic pattern of overlapping red and blue shifted gas (Case 3 in Figure 8), as discussed by Cabrit & Bertout (1 986). 1 ,ess inclined outflows present greater ambiguity, which partly explains why few reliable inclinations exist in the literature.

3.3.1. Comparison with CO spectral line outflow models

One method of assessing inclination and opening angles of **outflows** compares molecular spectral line data to theoretical models. Cabrit & Bertout (1 986,] 990) present models of the CO spectral line emission predicted from conical outflows. Figure 8 shows the regimes which correspond to the four different cases defined by Cabrit & 1 Bertout. Case 3 outflows lie in the plane of the sky, while Case 2 outflows have distinct red-shifted and blue-sllifted lobes, well-sc]mraled spatially. Case 1 outflows are observed almost, pole-on, and the red-shifted and blue-shifted lobes overlap. Case 4 outflows, which have very large opening angles, are rarely, if ever, observed. Cabrit & Bertout (1 986) talc.ulate the probability of observing an outflow with a given θ_{max}, and show that for $\theta_{max} \lesssim 20°$ (as is observed for TMC1 and TMC1A) the highest probability is found for Case 2. This is also demonstrated in Figure 8 by the possible solutions for those flows in the **Case** 2 region of the plot compared with Cases 1 and 3.

It is therefore most probable that TMC1 and TMC1A have Case 2 outflows, and to test this possibility further we compare CO position-velocity (P-V) diagrams obtained along the outflow axis with the theoretical diagrams calculated by Cabrit & 1 Bertout (I 986,] 990). Figure 9 shows the P-V diagrams obtained from our 8-channel averaged J CMT data, together with full resolution CO(2 1) spectra averaged over the mapped arm to demonstrate the S]1.3])[! Of the line wings. Close to the systemic velocity (marked by a solid vertical line) in both sources a combination of self- absorption by cool foreground material and emission in our off-positions serve to produce an artificial valley of low flux density.

Both our P-V diagrams and the integrated line profile correspond most closely k) the Case 2 models for an accelerated flow (Cabrit & Bertout] 986). Case 2 is defined by the geometrical constraints $i > \theta_{max}$, which gives spatially separated red and blue outflow lobes, and $i < 71/2 - \theta_{max}$, which constrains the flow to lie completely out of the plane of the sky.

The source inclinations and opening angles that satisfy both equation 2 and Case 2 appear as solid lines in Figure 8. The CO P-V diagrams allow us to exclude inclinations higher than 70° and 68° for TMC1 and TMC1 A respectively.

Cabrit & Bertout (1986, 1990) also compute maps of the integrated CO emission. We have not used these images to constrain further the inclination of TMC1 and TMC1 A, since we suspect that the computed spatial distributions may be sensitive to the outer cut-off radius assumed for the outflow cone. For example, an intrinsically short outflow length could be mistaken for a low inclination angle.

3.3..? *Comparison with near-infrared scattering outflow models*

Models of scattered near-infrared emission around protostars have successfully reproduced the observed conical structures (Whitney & Hartmann 1993). The models are sensitive to inclination, and may therefore be employed to constrain further the inclination. Whitney & Hartmann present model images that explore the effects of wind, envelope, and disk geometry on the structure of the near-infrared emission. There are three broad categories: low inclination objects dominated by a central point-source, similar to Case 1, moderate inclination sources displaying unipolar infrared reflection nebulae, and high inclination objects with bipolar infrared reflection nebulae, similar to Case 3. The near-infrared data for TMC1 and TMC1 A correspond most closely to their models 5 10 at $\sim 70°$ inclination. In general, the model images demonstrate very strong asymmetry at moderate inclinations. For i < 65° they find only the Heal-side (blue) lobe is visible. Our near-infrared data imply a slightly higher inclination because although the blue-shifted lobe is brightest, emission from both lobes is clearly present.

The near-infrared models, combined with the previous constraints, suggest TMC1 and

TMC1 A have inclinations between 65 and 70°. However, the near-infrared constraints are sensitive to the assumed density distribution of the circumstellar material, and the models rely upon high opacity in the envelope to attenuate emission from the far-side (red) lobe. The observed structure of the nebula and the infrared colors of the star could probably also be reproduced at other inclinations (1) by lowering the envelope opacity while increasing the extinction to the central star with a thick disk, or (2) by assuming noli-zero opacity within the stellar wind cavity. We therefore adopt $i > 40°$ as a conservative lower limit to our source inclinations. We conclude that the inclination of TMC1 is in the range of 40-70°, which implies a semi-opcming angle of 13-19°. Similarly, the inclination of TMC1 A is 40 68°, implying a semi-opmlilig angle of 1521°. The high ends of the limits are preferred by the models, and also by the statistical likelihood of a given inclination.

Several previous estimates of the inclinations of TMC1 and TMC1 A also exist. The spectral energy distribution analysis earl-ied out by Kenyon, Calvet, & Hartmann (1 993a) suggests inclination angles of 30° and 60° for 'J 'MC] and TMC1 A respectively, while Kenyon et al. (1993b) prefer inclination angles of 60 90° for both objects based on their scattered light imaging and)Ic.ar-infrared colors. This latter near-infrared study is consistent with our near-i nfrared discussion]] above. However, the fact that our deeper near-illfrared images do not exhibit strongly bipolar structure, along with the spectral line P-V diagram constraints, allow us to rule out very high inclinations.

3.4. The outflow cavity

Comparison of the data with the models shows several interesting features. First, the near-infrared images show limb-brightening that outlines the conical outflow cavity. Whitney & 11 artmann (1 993) suggest this effect can be produced by curvature in the cavity walls. Second, there is a notable difference between the theoretical P-V diagrams of Cabrit

& Bertout (1986) and our data. Figure 9 shows components associated with the front and back sides of each lobe, indicated by dot-dash lines. Emission at intermediate velocities is apparently suppressed, resulting in concave rather than convex contours. The modeling of Cabrit & Bertout (1986, 1990) assume the lobes are find with gas, and so do not show these feature.s. This further supports the suggestion that the lobes are evacuated of molecular material, in agreement with our near-infrared imaging. Third, the projected opening angle seen in the near-infrared images is larger than that found in the CO maps, particularly for TMC1 A. This is in qualitative agreement with the Whitney & Hartmann models, which show the reflection nebulosity to be larger than the (assumed) evacuated outflow cavity. More detailed modeling should be useful to constrain the ratio of the density inside and outside the outflow cavity.

4. Discussion

4.1. Conical structure

Molecular outflows vary greatly in their structure and physical characteristics, but they exhibit many common properties which theoretical outflow models must try to explain (Lada 1985; Masson & Chernin 1993; Stahler 1993). The conical shape near the central star displayed by TMC1 and TMC1 A (§ 3.1) is a relatively new feature, in part due to the small numbers of object, s which have been imaged in CO by millimeter interferometers, and the need to observe the youngest protostars.

Conical outflow structure is observed toward the Class 0 source 11335 in interferometer images (Chandler & Sargent 1993) and on a larger scale in single dish maps (Hirano et al. 1988). Mole recently, Bachiller et al. (1995) discovered the Class 0 source L1 448-(; exhibits a conical outflow cavity. 1,1448-(; also has a molecular jet (Bachiller et al. 1990), which

makes its similarity to TMC 1 and TMC1 A all the more interesting. However, TMC1 and TMC1 A have much weaker outflows, reflecting a factor of 3-4 smaller linear extent and velocity, and factor of 10-20 lower mass than the L1448-C molecular jet source.

The age of TMC1 and TMC1 A with respect to B335 and L1448-C is uncertain, but is important for comparison with theoretical outflow models. André et al. (1993) argue that Class O sources such as B335 and LI 448-~ are younger on average than Class 1 sources. However, TMC1 and TMC1 A are extreme Class 1 sources, which in this interpretation suggests their ages are not too much older than B335 and 1,1 448-C, and probably no more than 10^5 yr.

Other young low-mass sources observed in CO with interferometers include L1 6811], which shows a low-velocity jet, and L1262 and TMR-1, which have more complex, less collimated structure (Terebey et al. 1990; Terebey, Vogel, & Myers 1989, 1992). The high collimation of 1,168111 suggests it is very young, an interpretation consistent with its status as an extreme Class 1 source. However the properties of 1,1262 and TMR- 1 suggest they are older, as has been argued by Bontemps et al. (1 996). Taken together the observations imply that outflow cones are associated with the youngest protostars, and moreover, the limited statistics suggest conical structure is a common feature.

4.2. Evacuated cavity

The close correspondence of our near-infrared images with scattered light models which snow large extended structures (Whitney & Hartmann 1 993) provides the most convincing evidence for evacuated outflow cavities. In a near-infrared survey of the Taurus molecular cloud, Kenyon et, al. (1993b) argue that most embedded sources have low-opacity outflow cavities. Comparison of our much deeper near-infrared images for TMC 1 and TMC1A,

which clearly show spatially extended conical structure, with the scattering models of Whitney & Hartmann makes this interpretation compelling (§ 3.2 and 3.3.2), and further bolsters the contention that most embedded sources have evacuated outflow cavities. The evidence for evacuated cavities from molecular line data has been more controversial (Stahler 1993). However, in the case of TMC1 and TMC1A, the P-V diagrams of the CO(2- 1) data are consistent with the interpretation of an evacuated outflow cavity (§ 3.3.1).

The outflow cavity is evacuated in the sense that $\tau_{IR} \ll 1$ in the outflow, compared with $\tau > 1$ in the surrounding ambient gas. This suggests that the cavity is filled with low-density material. Alternatively, since dust provides the opacity, the outflow cavity could be filled by a high density but dust-free jet/w;ud. In this case, the near-infrared observations place strong constraints on the possible entrainment of ambient cloud material, and appear to rule out classes of models which turbulently mix ambient gas/dust into the outflow cavity, and thus produce a filled rather than evacuated outflow cavity (Cantó & Raga 1 W]; Stahler 1994).

4.3.   Moderate opening angles

For 'J 'MC1 and '1 'MC1A, the deprojected full-opening angles of the outflow cones are in the range 30-40°. There are also reliable opening angles in the literature for several systems whose high inclinations guarantee small deprojection corrections. The Class 0 sources 11335 and 1,1 448-C both have ~ 45° opening angles (Chandler & Sargent 1993; Bachiller et al. 1995). Observations of the prototypical Class O source VLA1623, also a molecular jet source, show a narrow 20 30° outflow opening angle (André et al. 1 990). For sources showing conical structure, which permits precise measurement of the opening angle, the data suggest typical values of 30 45° for the outflow opening angle. These values are significantly larger than the predictions of jet-driven outflow models (Masson & Chernin

1993).

4.4. CO line profile

The analyses of both Masson & Chernin (1992) and Stahler (1 994) use the observed form of mass as a function of velocity, $dM/dV \propto V^\gamma$ where $\gamma \sim$ - 1.8, to constrain the swept-up outflow mode] and the jet entrainment model. Indeed, the fact that the power-]aw index γ is similar in the sources measured so far, 1,1551 -11{.S5, NGC 2071, 111146-47 and VLA 1 623, has been used as an argument that the same acceleration mechanism is at work in those objects. Extending this analysis to our low luminosity so urces, the mass as a function of velocity derived from the J CMT data, assuming LTE, an excitation temperature of 20 K and optical ly-thin emission, also have $\gamma \sim$ - 1.8 if we fit a single power law (Figure 1 O). However, what is also quite clear is that a single power law is not a good mode] for the data, and if we were to insist upon fitting power laws, we would need at least two with very different slopes from the - 1.8 seen in other objects.

We note that in calculating the mass of high-velocity gas in outflows from CO spectra a single excitation temperature and optical depth for the entire line wing is almost always assu med. 'J 'his was the case for the three sources for WI rich γ was measured by M asson & Chernin (1992). This means that log-log plots of dM/dV vs. V are directly equivalent to log-log; plots of the line profile. Power laws have been fitted to the line wings in a number of other sources, including Orion-KL (Kuiper, Rodriguez Kuiper, & Zuckerman 1978), Cep A , and HL Tau (Rodríguez et al. 1982). The values of γ vary from - 1 .2 to - 2.1 in those objects, and like TMC1 and TMC1 A, the spectrum of Orion-KL is not well-modeled by a single power law. These results suggest that a power-law with $\gamma \sim$ 1.8 s} rould not be considered a universal feature of young outflows.

4.5.   Comparison with outflow models

Considerable observational evidence now exists that jets play an important role in driving outflows (e.g., Bachiller & Cernicharo 1990; Bachiller et al. 1990; Richer, Hills, & Padman 1992). There has been a corresponding theoretical push to explain molecular outflows and optical jets in terms of a unified model, based on the concept of a high-velocity neutral jet which drives the outflow (Stahler 1 993; Masson & Chernin 1 993; Raga et al. 1993). We suggest- the following properties are common features of young outflows which theoretical models should try to explain: 1) conical outflow lobes close to the star, 2) evacuated outflow cavities, and 3) moderate 30 45° opening angles.

The outflow models fall into the general categories of those driven by a radial stellar wind (Shu et al. 1991), and those driven by jets - either through shocks (Masson & Chernin 1 993; Raga et al. 1 993; Raga & Cabrit 1993) or through turbulent entrainment (Cantó & Raga 1991; Stahler 1994).

In the swept-up outflow proposed by Shu et al. (1991) and analyzed by Masson & Chernin (1 992) the outflow is driven by a radial stellar wind into the surrounding medium, and the shape of the outflow is defined by the distribution of the driving pressure and the column density of swept-up material. Shu et al. showed that the swept-up model could result, in the elongated outflows commonly observed, but Masson & Chernin argued that for reasonable distributions of the wind and cloud core the swept-up outflow model has problems reproducing plots of mass as a function of velocity. The cavity in this model is filled only with low-density material from the stellar wind. The swept-up wind II odel naturally reproduces the conical shape, evacuated cavity, and moderate opening angle suggested by observations. 1 lowever, to counter the objections raised by Masson & Chernin (1992) requires a near-spherical wind with a highly flattened density profile near the star to provide the collimation. Although this picture is possible, there is also the less desirable

effect that molecular bullets and optical stellar jets then have to be explained by a separate mechanism.

We next consider jet-drivml outflow models, in which a highly-collimated neutral jet drives the outflow and transfers momentum to the ambient medium through shocks. Masson & Chernin (1 993) treat the earliest stages of jet evolution, where momentum is transferred primarily through the leading bow shock, via a high-pressure cocoon of shocked gas which sweeps up ambient material as it expands away from the jet axis. A thin cocoon of swept up gas is identified with the molecular outflow. This class of models produces jets which arc too narrow, and too young (< 1 000 yr), although they can produce an evacuated outflow cavity (Chernin et al. 1994; Chernin & Masson 1995). A different approach was followed by Raga & Cabrit (1993), who treat the interaction of the bow shock with the ambient medium as a process of turbulent entrainment, leading to a thick cocoon of turbulent ambient material. Raga ct al. (J 993) propose a model appropriate. to the later stages of jet evolution, in which a time-variable jet produces many bow shocks along its length, leading to a turbulent envelope. The latter models can produce conical outflow structure close to the star, although the cone is still too narrow (Raga & Cabrit I 993; Raga et al. 1993,). However, the turbulent mixing generates a mostly filled rather than evacuated outflow cavity, cont rary to observations.

An alternative to shock acceleration is a situation where the acceleration of molecular gas is achieved through steady -sta(,c turbulent entrainment of ambient material along the edge of the jet (Cantó & Raga 1991 ; Stahler 1994). In the analysis presented by Stahler, which assumed the ambient medium to be of uniform density, the outflow would have a conical structure at low velocities, with the highest- velocity molecular gas loca ted closest to the jet axis. However, the 1 nodel produces a filled rather than evacuated outflow cavity. In addition, the model has difficulty reconciling observations of stellar jets with those of

molecular outflows (see Raga 1994).

Of our three constraints, jet models seem able to explain the conical shape near the star given a density gradient (Raga & Cabrit 1993; Raga et al. 1993), while the evacuated cavity can be produced in the momentun-conserving models which minimize turbulent entrainment (Chernin & Masson 1994). The most severe observational constraint is the moderate 30-45° opening angle, which is very difficult for jet models to reproduce. Masson & Chernin (1993) proposed a wandering jet to provide larger opening angles, a picture later elaborated as the wandering dentist drill (Chernin & Masson 1995). However, this scenario seems likely to produce messy outflow strut.tu res, rather than the symmetric cones that are observed around young sources. Recent models (Biro, Raga, & Cantó 1995) present an alternative implementation of the wandering jet hypothesis. Their 2-dimensional numerical simulation leads to a sinuous jet, with a different bow shock apparent at every S-shaped turn, very unlike the strut.ture of observed stellar jets. Further numerical modeling will be needed to determine whether jet models can reproduce the moderate opening angles observed towards you ng protostars.

4.6. Apparent acceleration along the outflow axis

The apparent acceleration of molecular material away from the exciting star has been observed in a number of sources (e.g., NGC 2071: Snell et al. 1984; 1,1551: Moriarty - Schieven & Snell 1988; Mon R2: Meyers-Rice & Lada 1991), but never before on the small scales we see for TMC 1 and TMC 1 A. A number of models seek to explain the phenomenon Meyers-Rice & Lada suggest that 'velocity - sorting' of clumps entrained by a wind or jet would result in the fastest-moving material being located at the largest distance from the source, giving rise to the observed velocity distribution.

The jet-cllt]ai~llt~cl)t model provides an alternative explanation (Stabler 1994), where the apparent acceleration is a column density effect. 1 ligh velocities exist at all radii, but the jet will have entrained more material at larger distances from the source, bringing its emission into the rail.ge of detectability. This requires the IIigIICXA-velocity material to be located along the jet axi s, and the outflow lobes to be filled with molecular gas. While the 1~igllcst-velocity emission is often also observed to be the most collimated (e.g., Richer et al. 19²2), this dots not necessarily indicate that the outflow has to be filled with molecular material; in projection, a hollow cone will have its highest radial velocities apparently more colli mated than lower-vclocit y gas.

Although the maxii num velocities observed in TMC1 and TMC1 A are relatively low ($\sim$ 30 km s] for an inclination angle of 60°) they are close to the limit at which molecules would be destroyed if the acceleration mechanism is a non-magnetic shock (30 50 km s¹: McKee & Hollenbach 1980). in this case trails-sollic or subsonic entrainment either by a wandering jet or by the bow shock may be essential in accelerating the molecular gas without causing excessive heating, so that the molecules are not destroyed.

5. Conclusions

1 ligl)-resolution imaging of the compact outflows associated with the sources TMC1 and TMC1 A in CO(1- O) shows that the outflows are conical down to sc.ales of 1000 AU, with the apex of the colic c.lose to the position of the millimeter conti nuum source in each Case. The dynamics of the flows, determined from CO(2- 1) data, indicate that they are low-luminosity versions of the more energetic outflows. Both the momentum flux and the mechanical luminosity of the flows follow the correlation between these quantities and the source bolometric luminosity determined by Cabrit & Bertout (1 992). A comparison of the $J= 2- 1$ transition with the 1- 0 gives a lower limit to the excitation temperature in the

line wing of 20 K, which is somewhat higher than the average temperature of molecular gas in the Taurus cloud (~ 10 1<). This suggests that the high-velocity gas has been heated locally, perhaps by the passage of a shock.

The conical structure of the outflows is also apparent in)Icar-infrared H and K images, which show extended near-infrared emission coincident with the 1~i~ll-velocity CO. Quantitative scattering models (Whitney & Hartmann 1 993) demonstrate that the lobes must be evacuated to explain the large spatial extent and structure of the extended lmar-infrared emission. In addition, the CO(2- 1) position-velocity diagrams show features corresponding to the front and back of a limb-brightened shell. These results for TMC1 and 'J 'M C1 A bolster the results of Kenyon et al. (1 993b) which suggest that most embedded sources have evacuat ed outflow cavities.

By comparing our P-V diagrams and line profiles with the outflow models of Cabrit & Bertout (1986, 1990) we constrain the inclination of both flows to the line of sight to be $i \lesssim 70°$. The inclination can be further limited by comparing the extended infrared reflection nebulosity with the Monte Cal 10 scattering models of Whitney & Hartmann (1 993), which suggest $i \gtrsim 40°$. This technique of combining near-infrared and CO observations can be used to determine inclinations toward other embedded infrared sources, especially those showing conical structure. The deprojected opening angles of the conical flows in TMC1 and TMC1 A are then 30 40°, similar to those observed in the Class O sources VLA1623, B335, and L1448-C (André et al. 1990; Chandler & Sargent 1993; Bachiller et al. 1995).

Taken together, the data suggest that the following properties are important for theoretical outflow models to explain, namely that young outflows have:

1) conical outflow lobes close to the star,

2) evacuated outflow cavities, and

3) moderate 30-45° opening angles.

None of the current outflow models satisfactorily explains the results. As found by Masson & Chernin (1992), outflows driven by radial stellar winds cannot reproduce the line profile with out unreasonably highly-flattened cloud cores. Steady-state turbulent jet models (Cantó & Raga 1991; Stahler 1994), where molecular gas is accelerated through turbulent entrainment along the edges of a collimated jet, produce a conical shape but a filled rather than evacuated cavity. Jet-dJ"iveJl bow shocks, in which a bow shock accelerates ambient material, in some cases can produce conical evacuated outflow cavities, but fail to reproduce the large opening angles and give ages which are too young (Masson & Chernin 1993; Raga & Cabrit 1993; Raga et al. 1993; Chernin & Masson 1995). Extending the jet model to include a wandering jet provides a possible way to provide large opening angles (Chernin & Masson 1995; Biro et al. 1995) but this possibility remains to be demonstrated.

Table 1. Outflow properties derived from CO(2-1) data.

		TMC1		TMC1A	
		Red lobe	Blue lobe	Red lobe	Blue lobe
M	$(M_\odot)$	1.2×10^{-3}	2.5×10^{-4}	$9.0 \times 10{-}4$	1.5×10^{-3}
V_{max}[a]	$(km\ s^{-1})$	15.4	9.2	11.9	13.6
$\langle V \rangle$[a]	$(km\ s^{-1})$	5.9	4.1	3.1	6.7
R	(m)	$1.3 \times 10^{'5}$	$6.3\ x\ 10^{14}$	$3.2\ x\ 10^{14}$	1.6×10^{15}
$t_{dyn} = R/V_{max}$	(yr)	2600	2200	840	3700
$P = MV_{max}$ $(M_\odot\ km\ s^{-1})$		$1.8\ X10{-}2$	2.3×10^{-3}	$1.1\ x\ 10{-}^2$	$2.0\ x\ 10{-}^2$
$F = MV_{max}^2/R$ $(M_\odot\ km\ s^{-1}\ yr^{-1})$		$7.1 x\ 10^{",\ G}$	1.0×10^{-6}	1.3×10^{-5}	5.5×10^{-6}
$E = MV_{max}^2/2$	(J)	$2.8 x\ 10{:}<[$	$2.1 x\ 10{:}3'1$	$1.3\ x\ 10^{35}$	$2.8\ x\ 10^{35}$
$L = MV_{max}^3/2R$	$(L_\odot)$	$8.8\ x\ 10{-}3$	$7.8\ x\ 10{-}4$	1.2×10^{-2}	6.1×10^{-3}
$\dot{M}_{outflow} = MV_{max}/R$	$(M_\odot\ yr^{-1})$	6×10^{-7}		1.5×10^{-6}	

[a] Assumes systemic velocity of 5.5 and 6.4 $km s^{-1}$ for TMC1 and TMC1 A, respectively.

'1'able 2. Outflow prop erties corrected for errors introduced duc to the lack of an opacity correction, based 011 the models of Cabrit & 1 Bertout (1 990).

Quantity X	$\log(X_{obs}/X_{cor})$	X_{obs}		X_{cor}	
		TMC1	TMC1A	TMC1	TMC1A
M $(M_\odot)$	-0.80	1.5×10^{-3}	2.4×10^{-3}	,9.5 X1O'3	1.5 X10-2
P ($M_\odot$ km S^{-1})	-0.55	2.0 X10-^{2}	$3,1$ X10-^{2}	7.1 x 10^{-2}	1.1 x 10^{-1}
F ($M_\odot$ km S^{-1} yr^{-1})	-0.55	8.1 XI O-G	1.8×10^{-5}	2.9 X10-S	6.4×10^{-5}
E (J)	-0.35	3.0 x 10^{35}	4.1 x 10^{35}	6.7 x 10^{35}	9.2×10^{35}
L ($L_\odot$)	-0.60	0.010	0.018	0.038	0.0'(2

REFERENCES

André, P., Martín-Pintado, J, Despois, D., & Montmerle, T. 1 W), A&A, 236, 180

André, P., Ward-Thompson, D., & Barsony, M. 1993, ApJ, 406, 122

Bachiller, R., & Cernicharo, J. 1990, A&A, 239, 276

Bachiller, R., Cernicharo, J., Martín-Pintado, J., Tafalla, h4., & Lazareff, 11. 1990, A&A, 231, 174

Bachiller, R., Guilloteau, S., Dutrey, A. Planesas, P., & Martín-Pintado, J. 1995, A&A, 299, 857

Bally, J., & Lada, C. J. 1983, ApJ, 265, 824

Biro, S., Raga, A. C., & Cantó, J. 1995, MNRAS, 275, 557

Bontemps, S., André, P., Terebey, S., & Cabrit, S. 1996, A&A, in press

Cabrit, S., & Bertout, C. 1986, ApJ, 307, 31 3

Cabrit, S., & Bertout, C. 1990, ApJ, 348, 530

Cabrit, S., & Bertout, C. 1992, A&A, 261, 274

Cantó, J., & Raga, A. C. 1991, ApJ, 372, 646

Chandler, C. J., & Sargent, A. 1. 1993, ApJ, 414, L29

Chernin, 1,., Masson, C., Gouveia Dal Pino, E. M., & Benz, W. 1994, 426, 204

Chernin, L. M., & Masson, C. R. 1995, 455, 182

Edwards, S., Ray, J., & Mundt, R. 1993, in Protostars and Planets 111, ed. E. H. Levy & J. 1. Lunine, University of Arizona Press, Tucson, p. 567

Elias, J. H., Frogel, J. A., Matthews, K., & Neugebauer, G. 1982, AJ, 87, 1 029

Heyer, M. H., Ladd, E. F., Myers, P. C., & Campbell, B. 1990, AJ, 99, 1585

Heyer, M. H., Snell, R. L., Goldsmith, P. H., & Myers, P. C. 1987, ApJ, 321, 370

Hirano, N., Kameya, 0., Nakayama, M., & Takakubo, K. 1988, ApJ, 327, L69

Kenyon, S. J., Calvet, N. & Hartmann, L. 1993a, ApJ, 414, 676

Kenyon, S. J., Whitney, B. A., Gomez, M., & Hartmann, L. 1993b, ApJ, 414, 773

Kuiper, T. B. H., Rodriguez Kuiper, E. N., & Zuckerman, B. 1978, ApJ, 219, 129

Lada, C. J. 1985, ARAA, 23, 267

Masson, C. R., & Chernin, L. M. 1992, ApJ, 387, L47

Masson, C. R., & Chernin, L. M. 1993, ApJ, 414, '230

McKee, C. F., & Hollenbach, D. J. 1980, ARAA, 18, 219

Meyers-Rice, B. A., & Lada, C. J. 1991, ApJ, 368, 445

Moriarty-Schieven, G. H., & Snell, R. L. 1988, ApJ, 332, 364

Murphy, D. C., & Myers, P. C. 1985, ApJ, 298, 818

Myers, P. C., Fuller, G. A., Mathieu, R. D., Beichman, C. A., Benson, P. J., Schild, R. E.,
    & Emerson, J. P. 1987, ApJ, 319, 340

Parker, N. D., Padman, R., & Scott, P. F. 1991, MNRAS, 252, 442

Raga, A. 1994, Ap&SS, 216, 105

Raga, A. C., Cantó, J., Calvet, N., Rodríguez, L. F., & Torrelles, J. 1993, A&A, 276, 539

Raga, A., & Cabrit, S. 1993, A&A, 278, 267

Richer, J. S., Hills, R. E., & Padman, R. 1992, MNRAS, 254, 525

Ricke, G. H., & Lebofsky, M. J. 1985, ApJ, 288, 618

Rodríguez, L. F., Carral, P., Moran, J. M., & Ho, P. T. P. 1982, ApJ, 260, 635

Shu, F. H., Ruden, S. P., Lada, C. J., & Lizano, S. 1991, ApJ, 370, L31

Snell, R. L. > Scoville, N. Z., Sanders, D. B. > & Erickson, N. R. 1984> ApJ, 284, 176

Stahler, S. W. 1993, in Astrophysical Jets, c{].]). Burgarella, M. Livio, & C. P. O 'Dea, Cambridge Univ. Press, Cambridge, p. 183

Stahler, S. W. 1994, ApJ, 422, 616

Tamura, M., Gatley, 1., Waller, W., & Werner, M. W. 1991, ApJ, 374, L25

Terebey, S., Beichman, C. A., Gautier, 'J'. N., & Hester, J. J. 1990, ApJ, 362, L63

Terebey, S., Chandler, C. J., & André, 1'. 1993, ApJ, 414, 759

Terebey, S., Vogel, S. N., & Myers, 1'. C. 1989, ApJ, 340, 472

Terebey, S., Vogel, S. N., & Myers, 1'. C. 1992, ApJ, 390, 181

Whitney, B. A., & Hartmann, 1,. 1993, ApJ, 402, 605

Fig. 1.- Channel maps of the CO emission from TMC1. *Left:* CO(1 - 0) imaged with the Owens Valley millimeter array. The LSR velocity is given at the top right hand corner of each panel, in km s^{-1}. Contours are spaced at 2σ intervals of *0.3* Jy beam^{-1}, starting at 0.3 Jy bear^{-1}. The asterisk denotes the continuum position given in Terebey et al. (1993). *Right:* CO(2- 1) emission obtained with the JCMT plotted to the same scale as the interferometer data, in the same velocity intervals. Contours are spaced at 2σ intervals of 4 Jy beam^{-1}, from a base level of 4 Jy beam^{-1}.

Fig. 2.- Same as Figure 1, for TMC1 A. *Left:* CO(I - O) imaged with the Owens Valley millimeter array. Contours are spaced at 1σ intervals of 0.4 Jy beam^{-1}, starting at the 2σ level of 0.8 Jy beam^{-1}. The asterisk is the position of the continuum source from Terebey et al. (1993). *Right:* CO(2- 1) emission from the JCMT. Contours are spaced at 3σ intervals of 6 Jy beam^{-1}, starting at G Jy beam^{-1}.

Fig. 3.- Interferometer maps of the integrated red- and blue-shifted CO(1- O) emission from TMC1 (left) and TMC1 A (ri.gilt), demonstrating the conical structure of the outflow lobes. The blue-sllifted gas is denoted by the solid contours, and the red-shifted gas is plotted as dashed contours. For TMC1, the blue-shifted emission is the 4.3 km s] (V_{LSR}) channel, with contours spaced at 0.3 Jy bear^{-1}. The red-shifted emission is an average of the three channels at 6.9, 9.5 and]2.] km s^{-1}, with contours 1.50 intervals of 0.13 Jy beam^{-1}, starting at the 30 level of 0.26 Jy beam 1. For TMC1 A, the 1~luc-shifted emission is an average of the three channels at - 3.2, - 0.6 and 2.0 km s^{-1} (V_{LSR}), with contours spaced at 0.4 Jy bear^{-1}, starting at 0.4 Jy beam^{-1}, and the red-shifted emission is the 7.2 km s^{-1} with contours as in Figure 2.

Fig. 4.- Integrated blue- and red-shifted CO(2- 1) emission, overlaid on a greyscale image of the high-velocity gas imaged by the interferometer in CO(1 0). The velocity intervals for the integration are the same as in Figure 3. Contour levels for the TMC1 blue lobe are the

same as in Figure 1 ; contour levels for the red lobe are at 5σ intervals of 6 Jy beam^{-1}. For TMC1 A the blue contours are at intervals of 8 Jy beam^{-1}, and the red Contours are at 30, 37, 40 and 43 Jy beam^{-1} .

Fig. 5.- Spectra of TMC1A in CO J= 1- 0 (thick line) and 2- 1 (thin line). The 1- 0 line is the spectrum obtained from the NRAO 12-111, and the 2- 1 is data obtained using the JCMT smoothed to the same spatial resolution. The dotted line is the ratio of 2-1 /1- 0 for those channels where the signal- to-noise ratio in both transitions was greater than unity.

Fig. 6.- Plot of the flux density ratio in the J= 2- 1 and 1- 0 transitions of CO, S_{21}/S_{10}, as a function of excitation temperature in LTE for various values of the J= 1- 0 optical depth. No solutions are possible for the line ratio in the region above the optically-thin limit. The dotted line shows the line ratio measured from the NRAO 12-m/JCMT data for TMC1 A, and the solid circle is the value obtained on much smaller scales from the JCMT and the Owens Valley interferometer measurements.

Fig. 7.- Contour plots of the near-infrared emission from TMC1 (top) and TMC1A (bottom) overlaid on greyscale images of the integrated high-velocity CO emission shown in Figure 3. On the left for each source is the H (1.6 μm) continuum, and on the right is the K (2.2 μm) continuum. The flux densities have been normalized to the photometry measured by Kenyon et al. (1993b), and contour levels are logarithmic at intervals of $\pm 1.5^n$ times 2.7 μJy arcsec^{-2} (TMC1, H-band), 3.1 μJy arcsec^{-2} (TMC1, K-band), 4.1 μJy arcsec^{-2} (TMC1 A, H-band), and 8.4 μJy arcsec^{-2} (TMC1A, K-band), where n = 0,1,2,3 . . .

Fig. 8.- Plot of the probability of different outflow geometries occuring for different combinations of inclination angle, i, and semi-opening angle, θ_{max}. The geometries for Cases 1, 2, 3, and 4 are defined by Cabrit & Bertout (1986), and are described in the text. The probability of observing a particular inclination for randomly oriented outflows is

proportional to $1 - \cos i$. The two lines marked TMC1 and TMC1 A show the solution of equation 2 for $\theta_{proj} = 20°$ (TMC1) and $\theta_{proj} = 22°$ (TMC1 A).

Fig. 9.- Positioll-velocity diagrams from the 8-channel averaged JCMT CO(2-1) data, obtained along the outflow axis for each source. Contours are equally spaced at 4 Jy beam^{-1} for TMC1, and 6 Jy beam^{-1} for TMC1 A. The dot-dash lines in each diagram denote features which correspond to the front and back side of each lobe. Spectra averaged over the whole mapped field with the full spectral resolution of the JCMT data are presented at the bottom of each plot, with solid vertical lines showing the systemic LSR velocity of the cloud in each case.

Fig. 10.- Plots of mass as a function of velocity for the red lobe of TMC1 (left) and the blue lobe of TMC1 A (right). V_0 is the systemic velocity of each source (i.e., 5.5 km s^{-1} for TMC1, and 6.4 km s^{-1} for TMC1 A). A power-law fit to the full data set, $dM/dV \propto V^\gamma$, is shown as the solid line in each case. Two-component power-law fits are al so displayed as dotted lines.
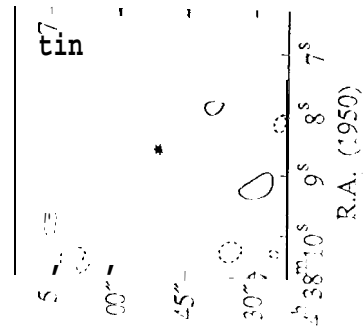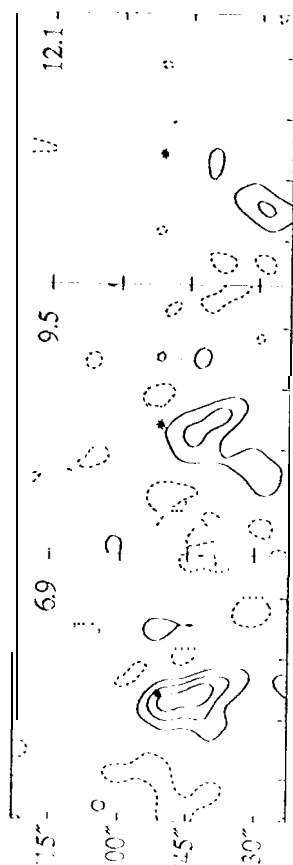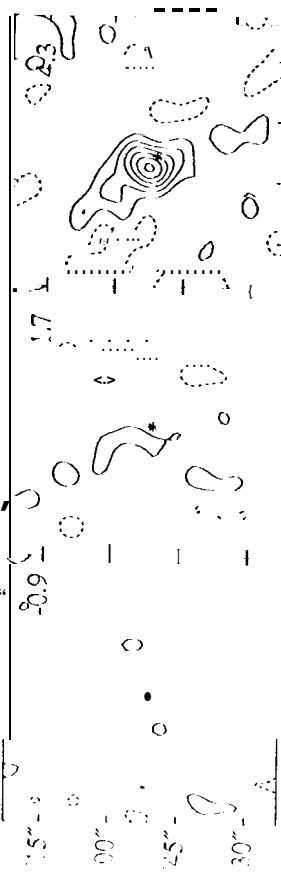
Figure 1b: TMC1 CO 2- JCMT

Figure 1a: TMC1 CO -0 OVRO

tin
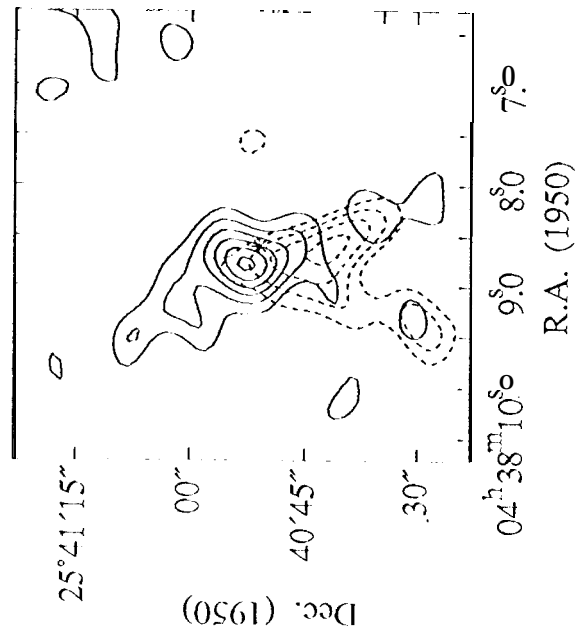
Figure 2b: TMC1A CO 2-1 JCMT
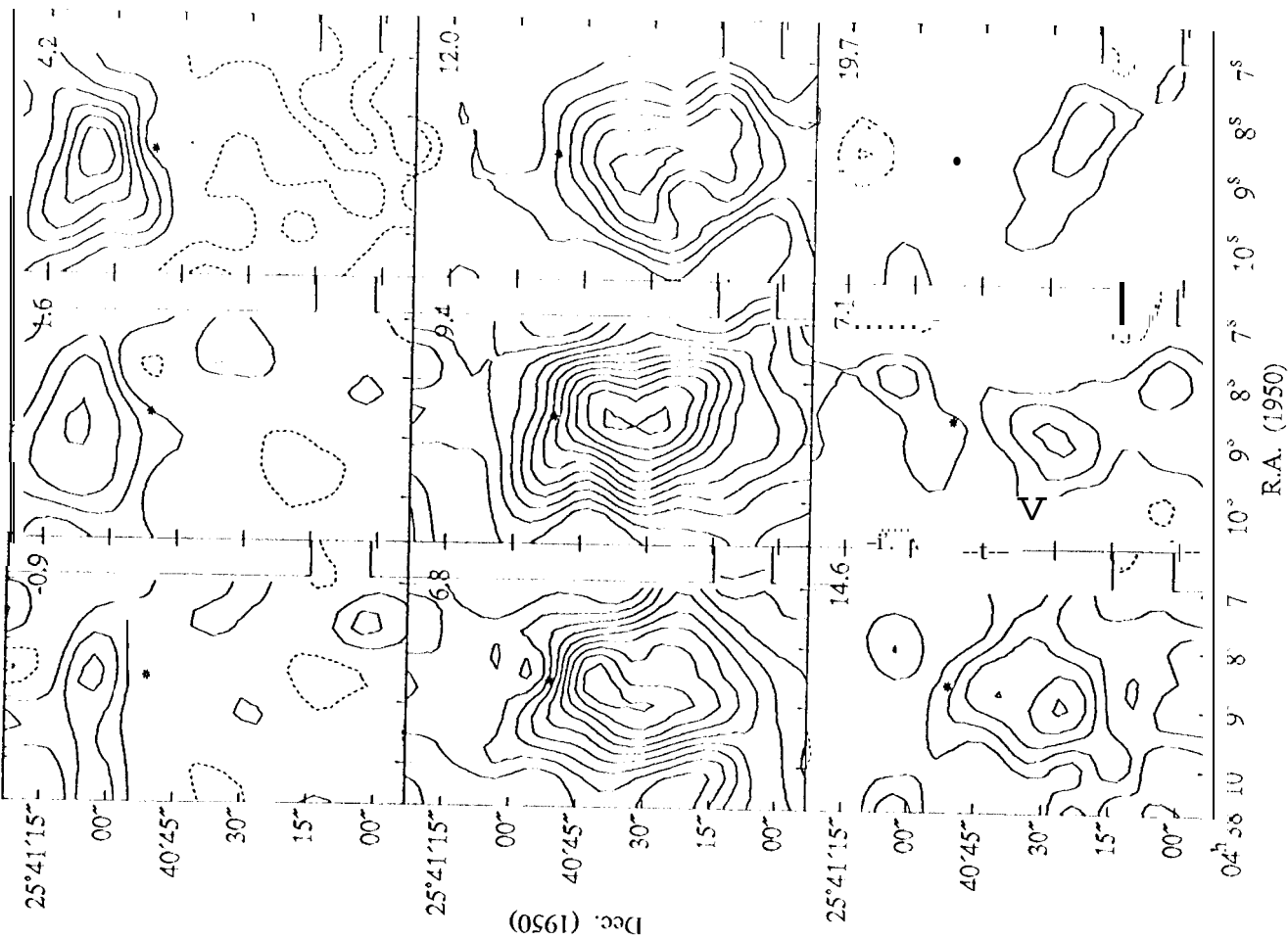
Figure 2a: TMC1A CO 1-0 OVRO
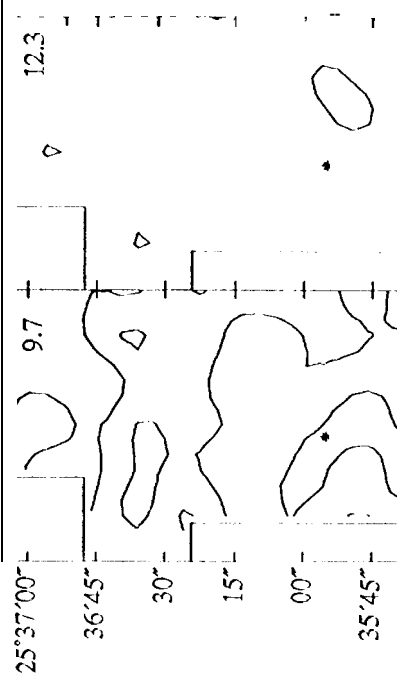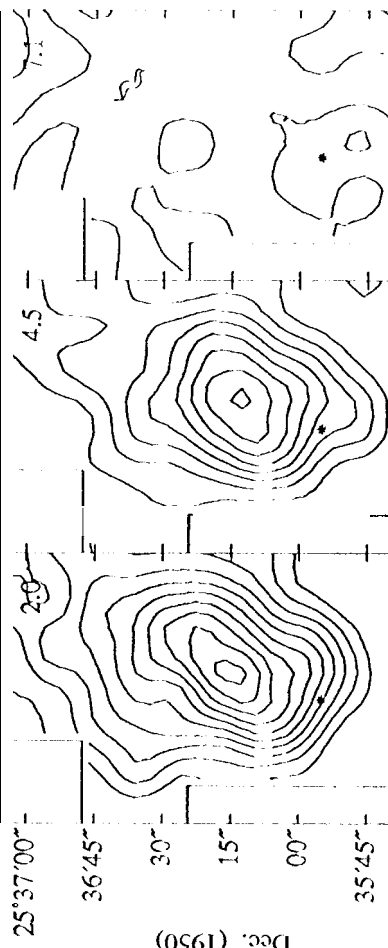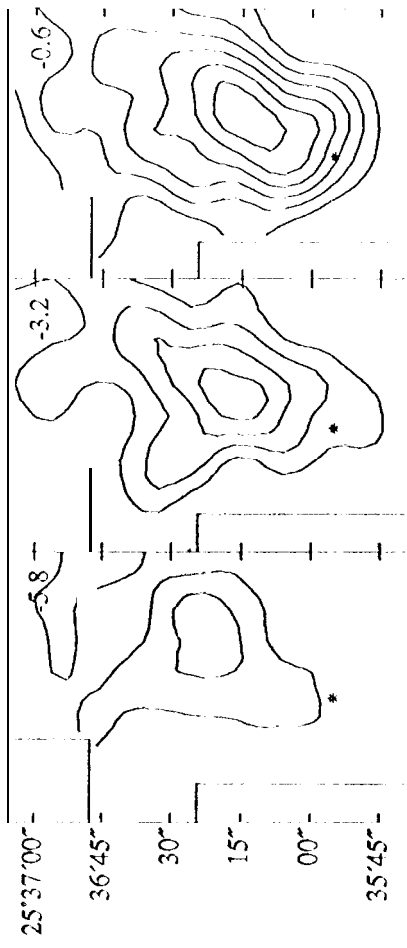
Figure 3a: TMC1

Figure 3b: TMC1A

Figure 4b: TMC1A

Figure 4a: TMC1

$J=1-0$

$J=2-1$

T_{21}/T_{10}

V_{LSR} (km s^{-1})

Fig. 7a: TMC1 outflow+} 1   Fig. 7b: TMC 1 outflow+K

25 °41'15"

00"

Dec. (950)

40"45"

30"

0 4^{11}38'"10!0 9^{S}0 8^{S}0 7^{S}0   10!0   9^{S}0 8^{S}0 7^{S}0

R.A. (1 950)

Fig. 7c: TMC1 A outflow+1 I   Fig. 7d: TMC1 A outflow+K

25 °36'15"

00"

Dec. (950)

35'45"

30"

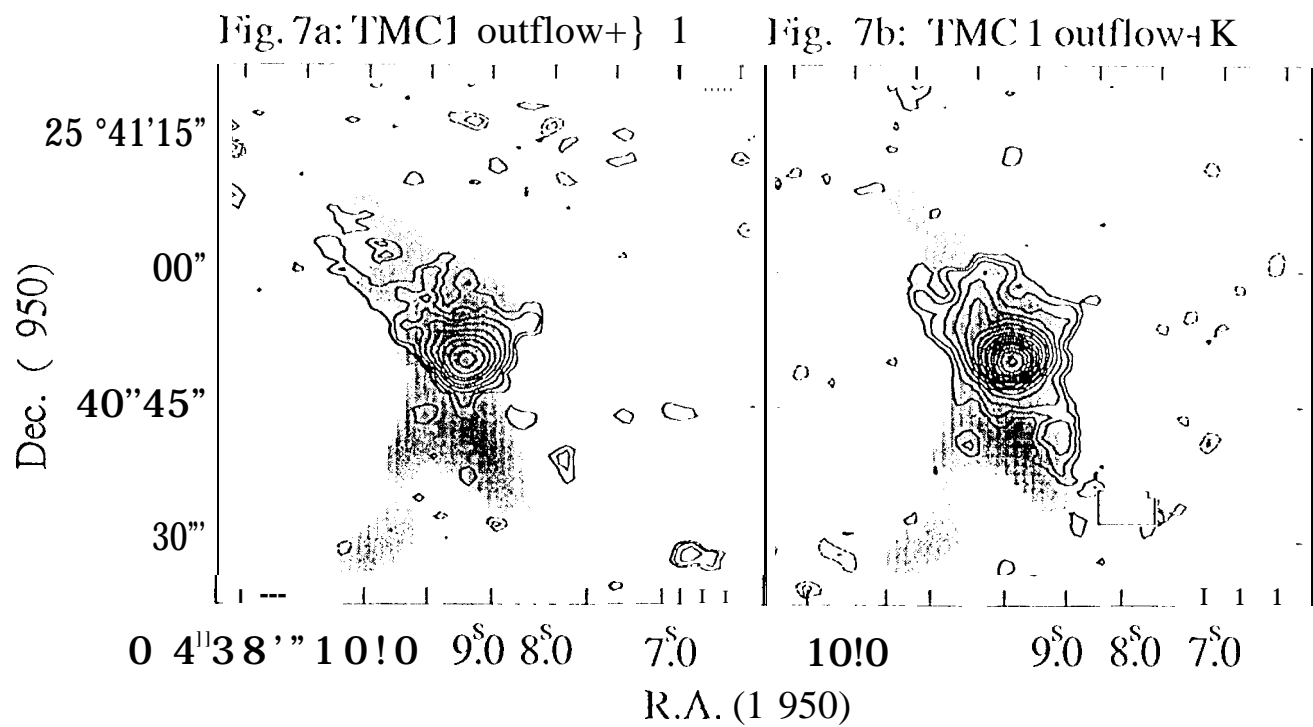04^{11}36^{m}33^{S}0 32^{S}0 31 ^{S}0 30^{S}0   33^{S}0 32^{S}0 31 ^{S}0 30^{S}0 29^{S}0
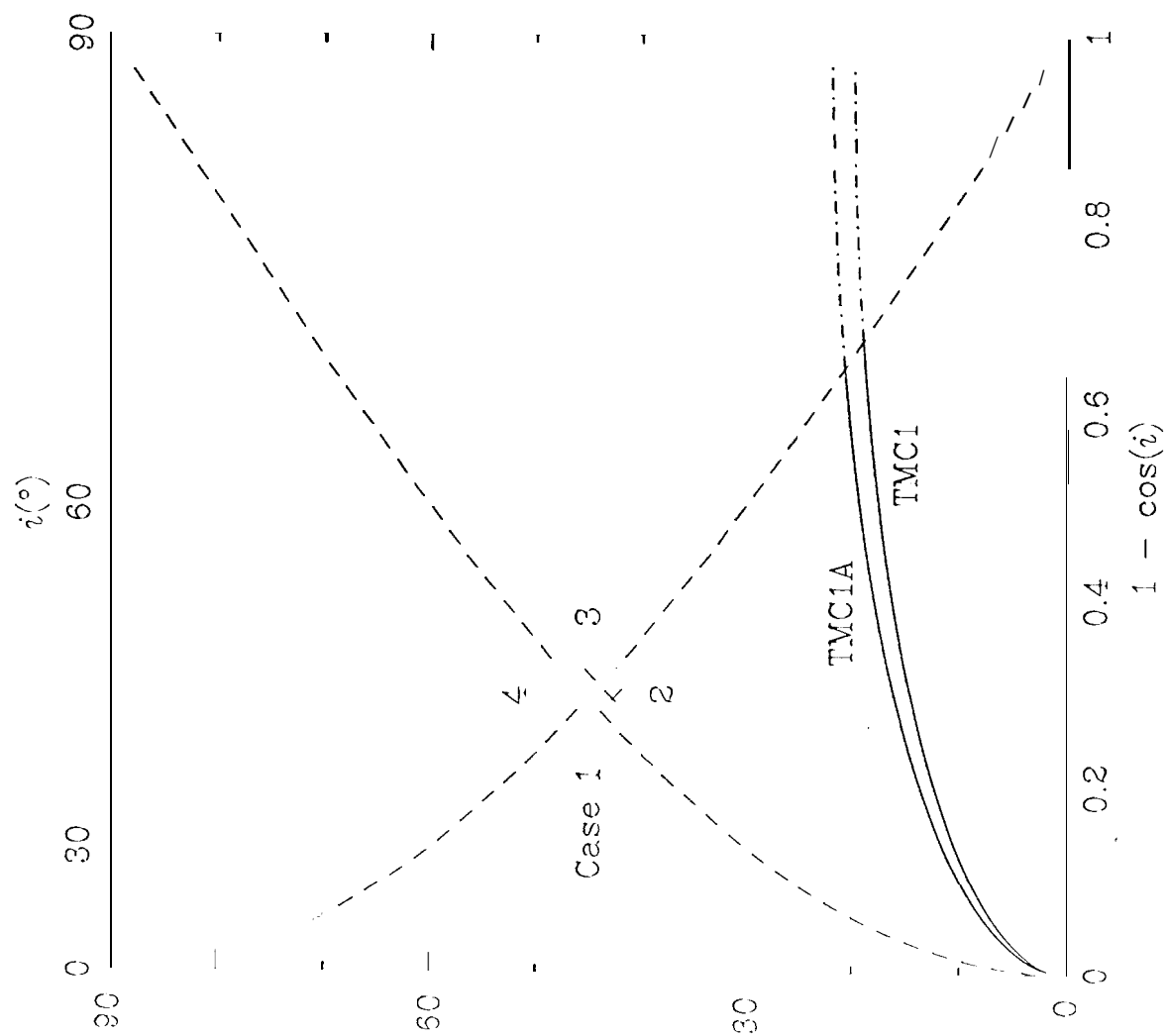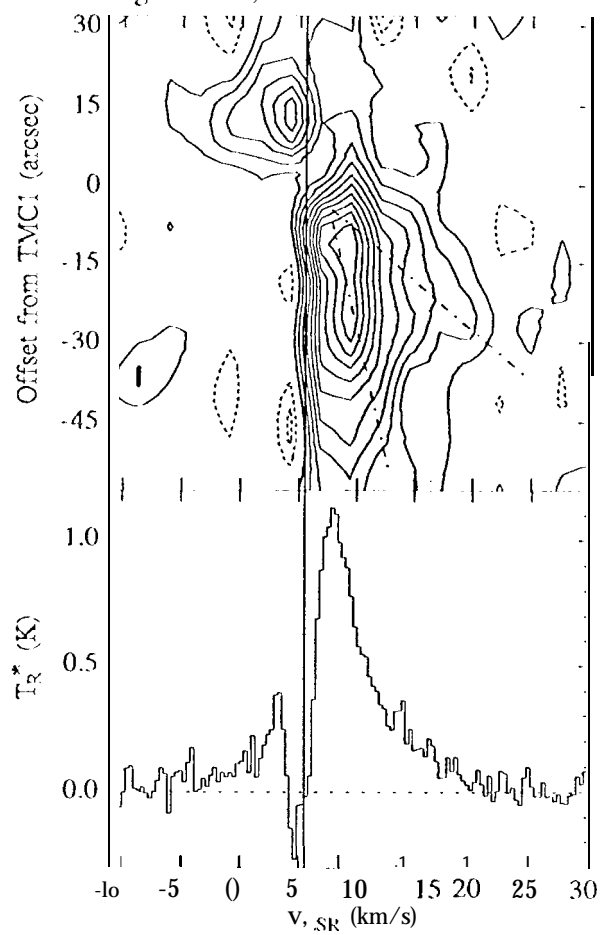
R.A. (1 950)
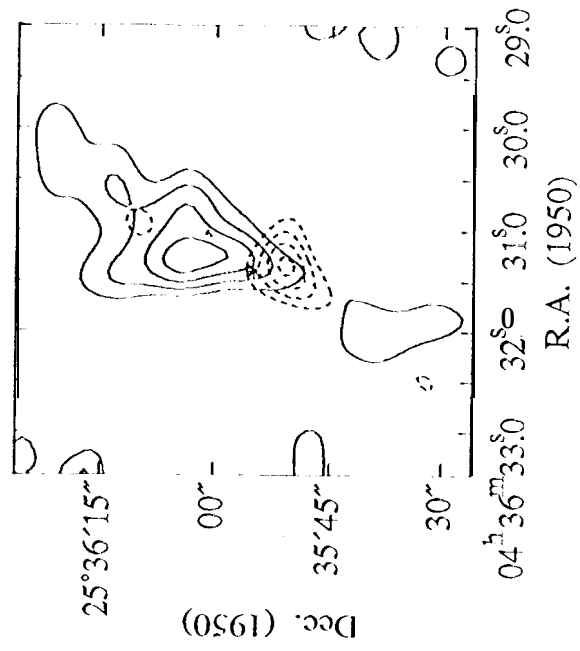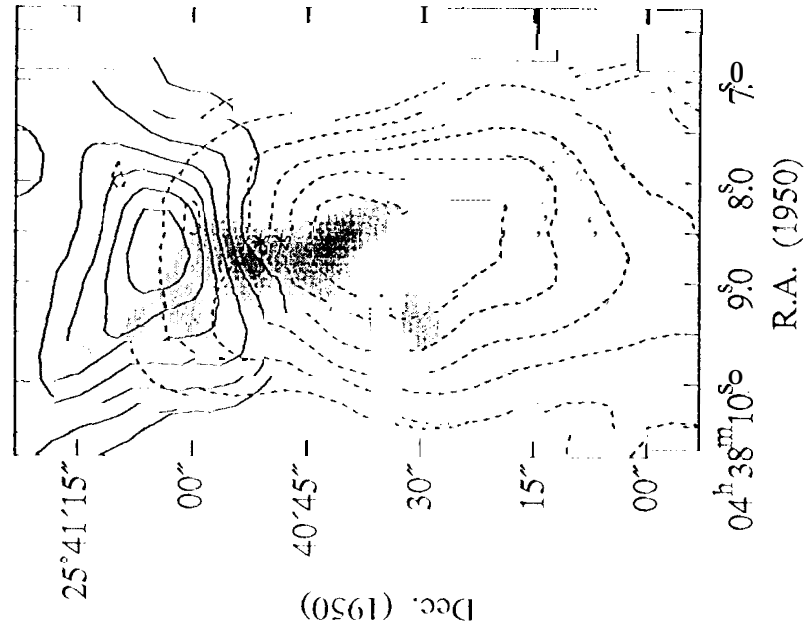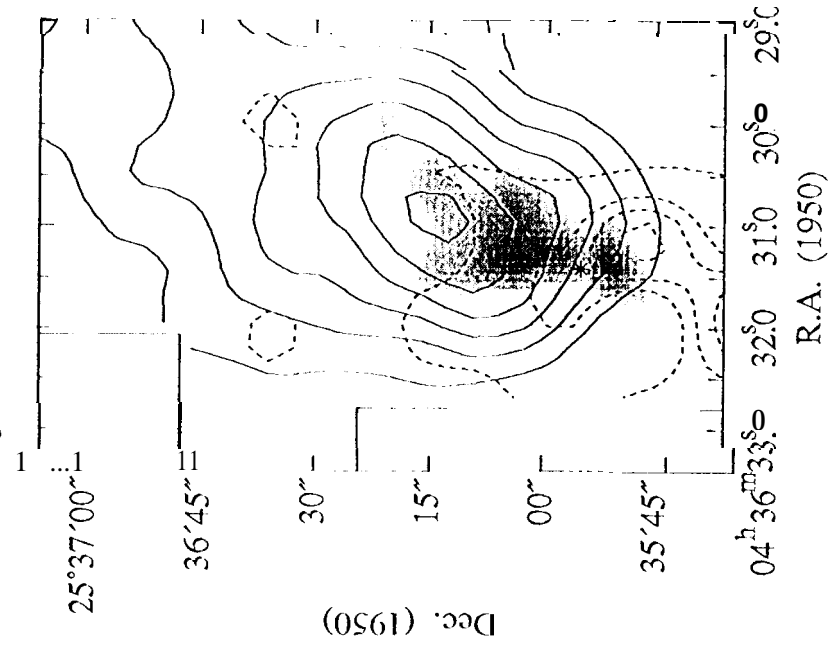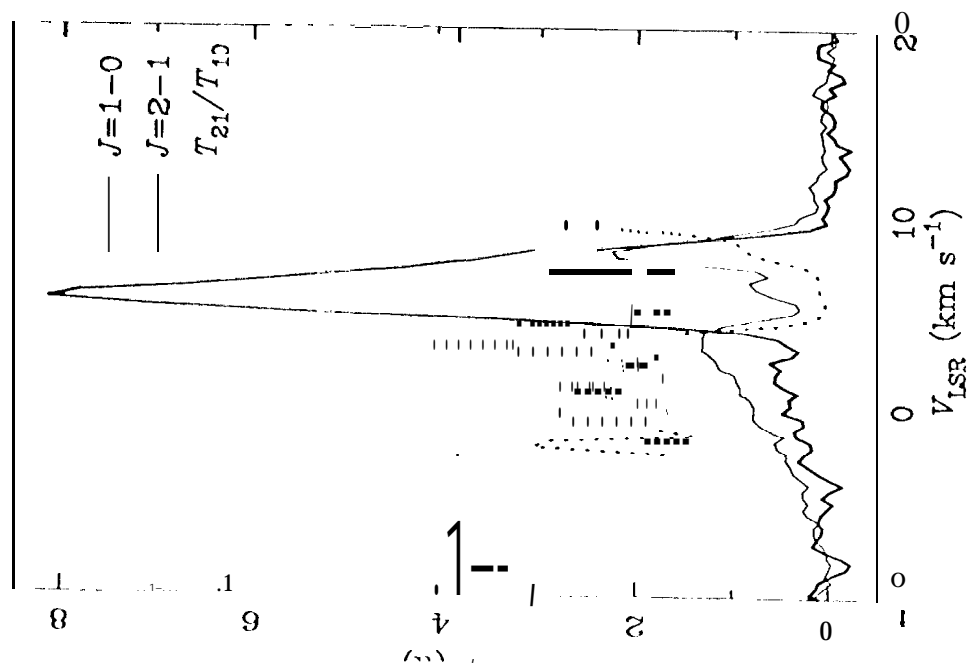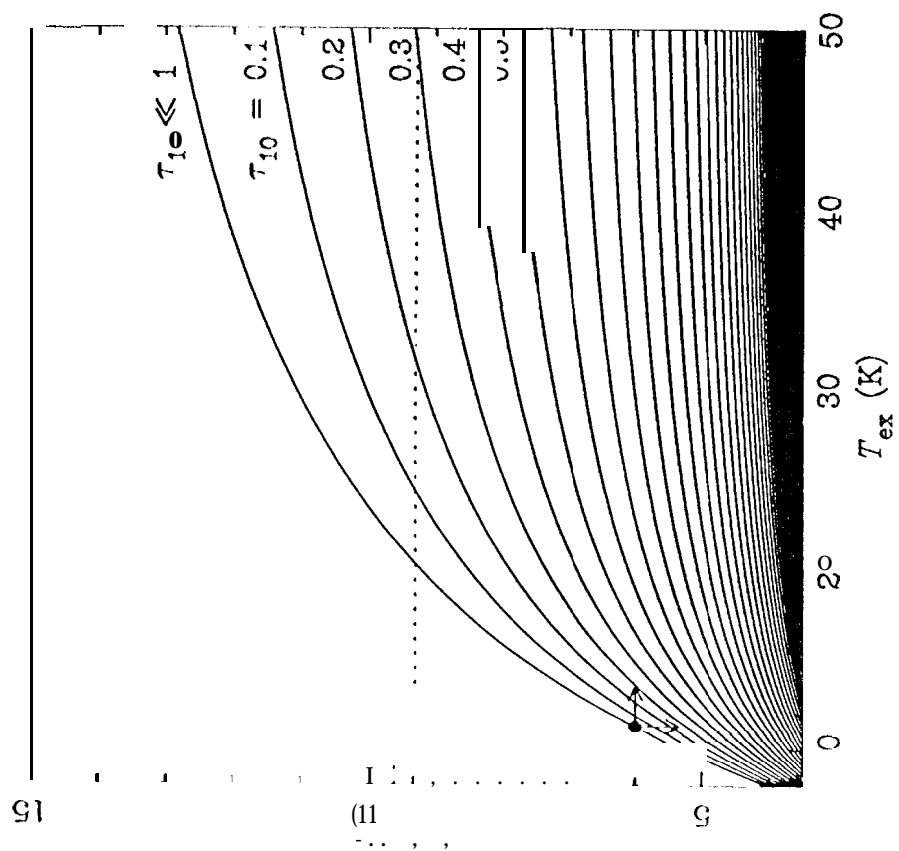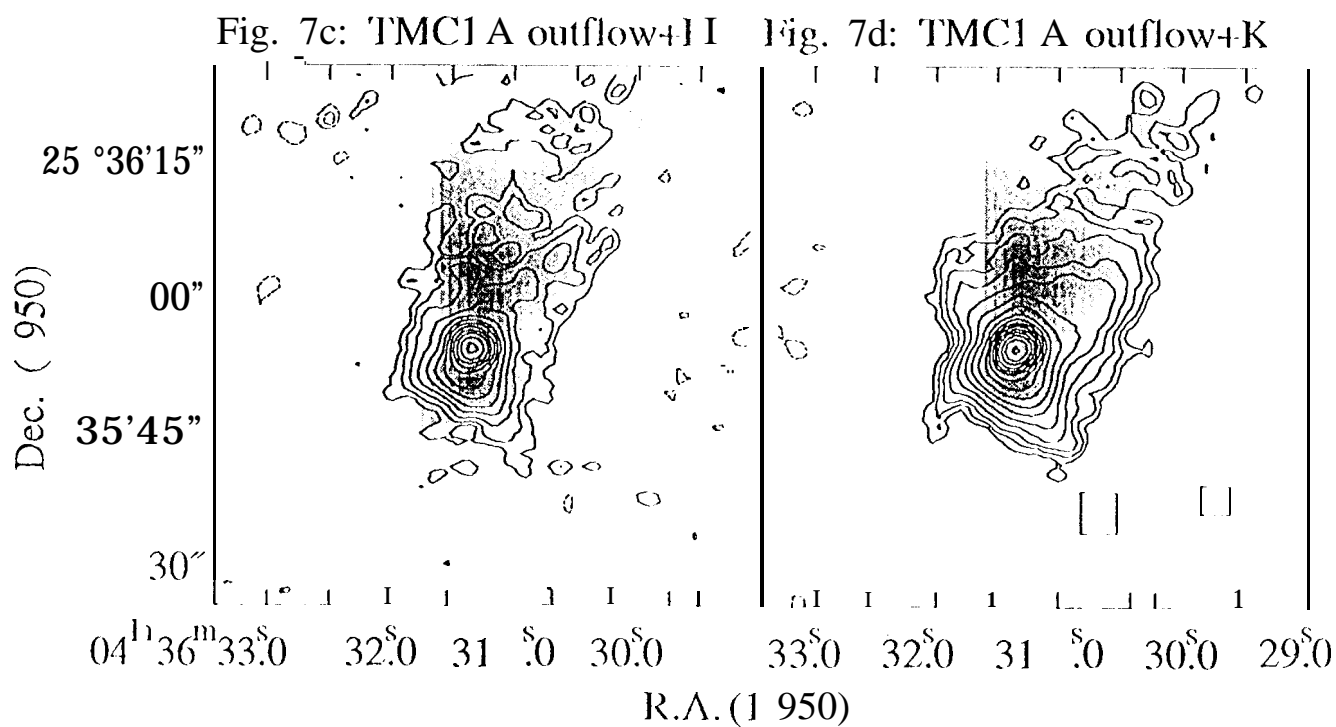
Fig. 9a: P-V, TMC1 outflow axis

Fig. 9b: P-V, TMC1A outflow axis

TMC1 red lobe

TMC1A blue lobe

$\gamma = 0.75$

$\gamma = -1.81$

$\gamma = -3.34$

$\gamma = -1.25$

$\gamma = -1.80$

$\gamma = -3.40$

log |V−V$_0$| (km s^{-1})